Causes and consequences of cellulose production by *Pseudomonas fluorescens* SBW25 at the air-liquid interface

Maxime Ardré[1,*] and Paul B Rainey[1,2,*]

[1]Laboratoire de Génétique de l'Evolution, Ecole Superieure de Physique et de Chimie Industrielles de la Ville de Paris (ESPCI Paris Tech), CNRS UMR 8231, PSL Research University, 75231 Paris, France.

[2]Department of Microbial Population Biology, Max Planck Institute for Evolutionary Biology, Plön 24306, Germany.

[*]For correspondence: maxime.ardre@espci.fr and rainey@evolbio.mpg.de

Keywords: diguanylate cyclase — bioconvection — pyoverdin — Raleigh-Taylor instability — continuum field models — ecological complexity

Running title: Cellulose and colonisation of the air-liquid interface

ABSTRACT

Cellulose over-producing wrinkly spreader mutants of *Pseudomonas fluorescens* SBW25 have been the focus of much investigation, but conditions promoting the production of cellulose in ancestral SBW25, its effects and consequences have escaped investigation through lack of *in vitro* phenotype. Here, using a custom built device, we reveal that in static broth microcosms ancestral SBW25 encounters environmental signals at the air-liquid interface that activate, via three diguanylate cyclase-encoding pathways (Wsp, Aws and Mws), production of cellulose. Secretion of the polymer at the meniscus leads to modification of the environment and growth of numerous micro-colonies that extend out from the surface. Accumulation of cellulose and associated microbial growth leads to Rayleigh-Taylor instability resulting in bioconvection and rapid transport of water-soluble products over tens of millimetres. Drawing upon data we build a mathematical model that recapitulates experimental results and captures the interactions between biological, chemical and physical processes.

IMPORTANCE This work reveals a new bacterial behaviour that manifests at the air-liquid interface, which depends on production of cellulose, and hints to hitherto unrecognised dimensions to bacterial life at surfaces. Additionally, the study links activation of known diguanylate cyclase-encoding pathways to cellulose expression and to signals encountered at the air-liquid interface. Further significance

stems from recognition of the consequences of fluid instabilities arising from surface production of cellulose for transport of water-soluble products over large distances.

51 **Introduction**

52 Surfaces are frequently colonised by microbes. Surface-associated
53 microbes grow as dense populations / communities termed "biofilms"
54 (1-3). Growth at surfaces provides microbes with nutrients and
55 opportunities for cross-feeding (4,5). For the pathogens surface
56 colonisation is often a prelude to invasion (6,7). Microbes in high-
57 density populations can find protection against external factors such
58 as antibiotics and toxic agents (8). At the same time, microbes in
59 biofilms experience intense competition for resources and can be
60 negatively impacted by costs associated with exposure to metabolic
61 waste products (9). For long-term survival, escape from surfaces and
62 dispersal is crucial (10).

63

64 Much attention has been given to colonisation of solid-liquid
65 surfaces (11,12). This owes as much to the importance of these
66 surfaces as it does the ease with which they can be studied. For
67 example, colonisation of abiotic surfaces can be measured by simple
68 histochemical assay or by microscopic observation using flow cells
69 (13,14). Decades of study have revealed much about adhesive factors
70 including polymers and proteinaceous adhesions involved in surface
71 attachment and the regulatory pathways controlling their expression
72 (15). A particular focus has been pathways for synthesis and
73 degradation of the secondary signalling molecule cyclic-di-GMP (16).
74 For the most part, the precise signals activating these regulatory
75 pathways are unclear. Moreover, the frequent use of mutants —

76 sometimes intentionally but often inadvertently — that constitutively
77 over-produce adhesive factors has stymied progress in understanding
78 many subtleties surrounding surface colonisation.
79
80 Surfaces are also a feature of the interface between gas and liquid,
81 but colonisation of such surfaces has been little studied (17,18).
82 Air-liquid interfaces (ALIs) are of special relevance for aerobic
83 organisms because colonisation of the meniscus provides access to
84 oxygen that is typically absent from the broth phase. While many
85 motile aerobic bacteria display taxis toward oxygen, this alone may
86 be insufficient to allow cells to contend with the forces required to
87 overcome the effects of surface tension and colonise the meniscus.
88 Once achieved, in the absence of mechanisms to achieve buoyancy,
89 cells growing at the interface must contend with the effects of
90 gravity.
91
92 The interface between air and liquid has further significance in that
93 it often marks the divide between aerobic and anaerobic conditions.
94 This has implications for surface chemistry with ensuing
95 physiological effects for bacteria. For example, iron, an essential
96 element, exists in the insoluble and biologically unavailable ferric
97 form in the presence of oxygen, but is water soluble and freely
98 available in the absence of oxygen (19). Bacteria growing within an
99 initially resource-rich and oxygen replete broth phase consume oxygen
100 and thus further growth requires access to the ALI (20). Bacteria

101 that achieve colonisation of this surface must then contend with iron
102 deplete conditions requiring the synthesis of siderophores (21).
103
104 To date, studies of colonisation of the ALI have been largely centred
105 on genotypes that constitutively produce polymers such as cellulose
106 (22). Often these have arisen as a consequence of selection
107 experiments in static broth microcosms where mutants with
108 constitutively active diguanylate cyclases (and ensuing constitutive
109 production of the respective polymers) have a selective advantage
110 that arises from capacity to form a dense microbial mat at the air-
111 liquid interface (23-25). While such mutants have made clear the
112 central importance of cellulose and related polymers the generality
113 of conclusions arising from the use of constitutively active mutants
114 need to be treated with caution (24). Desirable would be analysis of
115 the biophysics of ALI colonisation in wild type bacteria where
116 regulation of polymer production is unaffected by mutation.
117
118 Almost two decades ago it was reported that in well-mixed culture the
119 fitness of a cellulose-defective mutant of *Pseudomonas fluorescens*
120 SBW25 was equivalent to that of the wild type (ancestral) bacterium
121 (22). Also reported in that study was a significant reduction in
122 fitness of a cellulose defective mutant in static broth culture, but
123 the reasons were not determined. Recent observations of the growth of
124 a cellulose-defective mutant of wild type (ancestral) SBW25 made
125 during the course of analyses of evolutionary convergence in polymer

126 production by SBW25 (26) led to the realisation of a subtle phenotype
127 associated with absence of growth in the cellulose-defective mutant
128 at the air-liquid interface. Unlike ancestral SBW25, it grows
129 exclusively within the broth phase with ensuing negative effects of
130 oxygen limitation responsible for its previously noted low fitness
131 (22).
132
133 Here we seek to understand the biological role of cellulose and do so
134 via a device that combines spectrophotometry with multi-perspective
135 time-lapse imaging. Aided by the device we monitor surface growth,
136 reveal the contribution made by cellulose and show that it involves
137 regulatory contributions from three known diguanylate cyclase-
138 encoding regulatory pathways. The production of cellulose allows
139 formation of a lawn of micro-colonies at the meniscus that eventually
140 coalesce into a thin film of bacteria. The mass of bacteria and
141 cellulose generates a gravitational force that leads to Rayleigh
142 Taylor instability and causes bioconvection (27). One consequence of
143 bioconvection is the rapid transport of the water-soluble iron-
144 binding siderophore, pyoverdin. A mathematical model based on
145 partial differential equations with fluid dynamics described by the
146 Navier–Stokes (NS) equation with Boussinesq approximation accounts
147 for the diffusion-reaction and convection processes occurring in the
148 microcosm.
149
150

151 **RESULTS**

152 Describing microbial colonisation of the air-liquid interface
153 (hereafter ALI), although in principle straightforward, is fraught
154 with difficulty. While advanced microscopic techniques offer
155 possibilities to observe colonisation at the single cell level, much
156 stands to be gained from more macroscopic perspectives, aided by low
157 power microscopy in conjunction with time-lapse photography.

158

159 **Device.** To understand and quantitate growth of ancestral SBW25 and
160 the cellulose-defective mutant SBW25 Δ*wssA-J* a device was constructed
161 that allows growth at the ALI and in the broth phase to be monitored
162 from multiple perspectives (Fig. 1). It comprises three cameras: one
163 placed perpendicular to the microcosm to record growth within the
164 microcosm and on the under surface of the meniscus, one mounted at a
165 45° angle above the ALI to capture surface growth and one to detect
166 the light emitted from excitation of the fluorescent signal arising
167 from production of the iron-chelating siderophore, pyoverdin.
168 Additionally, the device incorporates a laser and corresponding
169 photodiode to vertically scans the flask at regular (5 min) time
170 intervals.

171

172 **Cellulose is required for colonisation of the ALI.** Figure 2 shows the
173 growth dynamics of ancestral SBW25 and SBW25 Δ*wssA-J* determined by
174 the scanning laser and calibrated using direct plate counts. SBW25
175 Δ*wssA-J* is slower to enter exponential growth than SBW25, it grows at

176 approximately the same rate (SBW25, 0.53+/-0.02 h^{-1}; SBW25 Δ*wss*A-J
177 0.57+/-0.03 h^{-1}), but density in stationary phase is consistently
178 lower. Notable in SBW25 at ~24 hours is a reproducible plateau of
179 growth followed by a further increase and a widening of difference in
180 cell density compared to SBW25 Δ*wssA-J* (Fig. 2). No such
181 intermediate plateau occurs in the cellulose mutant.
182
183 Time-lapse observation of the ALI from a 45° angle in flasks
184 inoculated with SBW25 reveal presence of a thin film at 19 h that is
185 more prominent at 26 h and still evident albeit weakly at 40 h (Fig.
186 3a and supplementary movie file 1). In contrast, no evidence of
187 colonisation of the ALI is evident in SBW25 Δ*wssA-J* (Fig. 3b and
188 supplementary movie file 2). Observations from the camera
189 perpendicular to the flasks confirmed presence of surface growth in
190 SBW25 (Fig. 3a), but not in the cellulose mutant (Fig. 3b).
191 Additionally rapid streaming was observed in the broth phase for the
192 ancestral genotype but not for SBW25 Δ*wssA-J* (Fig. 3a and 3b,
193 supplementary movie files 3 and 4 respectively). The significance of
194 this streaming dynamic is considered in detail below.
195
196 Curious as to the nature of the previously unseen surface growth we
197 obtained high-resolution photos at hourly intervals (between 15h and
198 20 h) from directly above the surface using a light source for
199 illumination positioned at an oblique angle to the surface. No
200 surface growth was evident for SBW25 Δ*wssA-J* (Fig. 4b), but

201 remarkably, from the ancestral genotype, numerous micro-colonies
202 emerged from the surface of the meniscus and grew outward as if on an
203 agar plate (Fig. 4a). By 19 hours the micro-colonies coalesced into a
204 single structure (Fig. 4a) that upon coalescence collapsed
205 (supplementary movie file 5).
206
207 **Regulation of cellulose and ALI colonisation by multiple diguanylate**
208 **cyclase-encoding regulatory pathways.** Numerous studies of
209 constitutive cellulose over-producing mutants — the so named wrinkly
210 spreader (WS) types (28) — have shown the phenotype to arise
211 primarily by mutations in the Wsp, Aws and Mws pathways (25-30).
212 Mutations in the negative regulators of these diguanylate cyclase-
213 encoding pathways (DGCs) result in over-production of cyclic-di-GMP,
214 over-production of cellulose and formation of substantive and
215 enduring mats at the ALI. While these findings have connected *over-*
216 *expression* of DGC-encoding pathways to the WS phenotype, the
217 relationship between known DGC-encoding pathways and cellulose
218 expression in the absence of DGC over-activating mutations has been a
219 mystery. Recognition that ancestral SBW25 activates cellulose
220 production at the ALI leading to micro-colony formation and a frail
221 film of cells, allowed investigation of the role of Wsp, Aws and Mws
222 in expression of this phenotype.
223
224 A reduction in the formation of micro-colonies in SBW25 Δ*wspABCDEFR*,
225 SBW25 Δ*awsXRO*, and SBW25 Δ*mwsR* demonstrates for the first time a

226 connection between the Wsp, Aws and Mws pathways, the production of
227 cellulose and colonisation / micro-colony formation at the ALI (Fig.
228 4c). Surprisingly, no single pathway mutant resulted in a cellulose
229 defective phenotype that matched that of the cellulose defective
230 *wssA-J* deletion mutant (Fig. 4c). Equally surprising was that all
231 three pathways make some contribution to colonisation of the ALI
232 (Fig. 4c). The most pronounced phenotype was associated with SBW25
233 Δ*mwsR*, followed by SBW25 Δ*awsXRO* and SBW25 Δ*wspABCDEFR*. A mutant
234 lacking all three pathways was indistinguishable from SBW25 Δ*wssA-J*
235 (Fig. 4c).
236
237 **Cellulose causes bioconvection**. As noted above, in microcosms
238 inoculated with cellulose-producing ancestral SBW25, material falls
239 in finger-like plumes that stream from the ALI (Fig. 3a). Analysis of
240 time-lapse movies (supplementary movie file 6) shows plumes to be
241 characteristic of long-range convection (Fig. 5), which arises as a
242 consequence of instability of the interface between the cellulose-
243 rich meniscus and the less dense broth phase beneath. The phenomenon
244 is known as Rayleigh-Taylor instability. That cellulose is the
245 critical component stems from the fact that the streaming plumes are
246 evident in ancestral SBW25, but not in cultures of the cellulose
247 negative mutant (SBW25 Δ*wssA-J*).
248
249 Quantification of the streaming plumes shows instability at ~25 h and
250 continues until ~40 h at which point streaming ceases and the medium

251 becomes homogeneous. The velocity of the falling plumes ranges from
252 500 to 2000 $\mu m \cdot min^{-1}$ (Fig. 5). From this it is possible to calculate
253 the Péclet number that defines the contribution of diffusion relative
254 to bioconvection on the transport of water-soluble products. In this
255 instance the Péclet number (*Pe*) is ~1,000 (calculated by multiplying
256 the typical plume length (1 cm) by its velocity ($\sim 1 \cdot 10^{-3}$ $cm \cdot s^{-1}$) and
257 then dividing by the diffusion coefficient of pyoverdin $\sim 1 \cdot 10^{-6}$ $cm^2 \cdot s^{-}$
258 ^{1}). The Péclet number, being greater than 1 (*Pe* is a dimensionless
259 number), means that bioconvection is a more significant contributor
260 to the transport of soluble products than diffusion.
261
262 **Bioconvection affects spatial distribution of extracellular products.**
263 A soluble product of relevance to *P. fluorescens* SBW25 in static
264 culture is the water-soluble iron binding siderophore, pyoverdin
265 (31). That it is fluorescent means that it is readily monitored.
266 Figure 6a shows the average concentration of pyoverdin at the ALI as
267 imaged via camera 2 equipped with suitable optical filters (see Fig.
268 1). The first indication of pyoverdin production occurs at the ALI at
269 ~19 h and coincides precisely with the first visible stages of
270 surface colonisation where micro-colonies begin to form at the
271 meniscus (Fig. 4).
272
273 The first signs of pyoverdin production are restricted to the ALI
274 despite the fact that at 19 h and thereafter, the broth phase is
275 turbid with growth (supplementary movie file 3 shows turbidity in the

276 flask and supplementary movie file 7 shows pyoverdin in the flask).
277 This is consistent with oxygen being available at the broth surface
278 (and absent in the bulk phase due to metabolic activity) causing iron
279 at the ALI to exist in the insoluble ferric form, leading to
280 activation of pyoverdin synthesis solely at the ALI. The kinetics of
281 pyoverdin production were quantified by fitting data to a simple
282 logistic model (Fig. 6a) whose fit indicates that the underlying
283 chemical reaction is autocatalytic and characteristic of positive
284 feedback regulation that controls pyoverdin synthesis (31).
285
286 Visible plumes of pyoverdin (Fig. 6b) were quantified by measuring
287 pixel intensity across a single horizontal profile (inset Fig. 6c) as
288 indicated by the red line in Figure 6b. To determine the
289 characteristic plume width (Fig. 6c), the data were analysed by Fast
290 Fourier transformation (FFT). The transformation shows that pyoverdin
291 is concentrated in plumes with a horizontal width of 3mm.
292
293 **Modelling microcosm dynamics**. Surface colonisation by *P. fluorescens*
294 SBW25, interaction of cells with oxygen and ensuing effects,
295 including bioconvection and transport of pyoverdin, draw attention to
296 striking ecological complexity in this simplest of microcosms. To
297 determine the match between current understanding of the interplay
298 between biological, chemical and physical processes and the extent to
299 which simple biophysical mechanisms explain the observed dynamics, we
300 constructed a model based on diffusion-reaction processes and

301 hydrodynamics. The degree of fit between model and data stands to
302 show how well the system is understood.
303
304 The model is based on experimental quantification of bacterial
305 density, pyoverdin concentration, and fluid flow. It uses partial
306 differential equations to account for the diffusion-reaction-
307 convection processes within in the flask. The local concentration of
308 bacteria, oxygen, pyoverdin and cellulose are described as continuous
309 fields. The liquid environment is modelled as an incompressible
310 Newtonian fluid with a mass density that depends on the
311 concentrations of bacteria and cellulose. Its dynamic is described by
312 the Navier–Stokes (NS) equation using the Boussinesq approximation,
313 in which the variations of density are neglected except in the
314 buoyancy force (32). The coupled equations allow for inclusion of
315 different physical interactions between the components. Details are
316 provided in the Materials and Methods section.
317
318 The model was solved numerically as a means of validation.
319 Simulations were performed on a two-dimensional grid representing a
320 physical domain of size 1 cm^2. The top of the domain corresponds to
321 the ALI with free fluid slip (liquid can move along the ALI) and no
322 penetration boundary conditions (the meniscus cannot be deformed).
323 The sides correspond to the lateral walls of the microcosm and the
324 bottom of the flask. The boundary conditions on the wall allow no
325 fluid slip (liquid cannot move along the wall) and no penetration.

326

327 The results of the simulation are showing in Figure 7 (and
328 supplementary movie files 8-11) and closely reproduce the dynamics
329 observed in microcosms. Bacteria replicate and consume oxygen until
330 growth saturates at ~$3 \cdot 10^8$ cfu·ml^{-1}. At 16 h oxygen is available at
331 the meniscus and in a single millimetre layer immediately below the
332 ALI. Also at 16 h pyoverdin production begins; at 19 h the first
333 indication of cellulose production become visible resulting in an
334 increase in density of the surface layer. Soon after, cellulose-
335 laden regions begin to form descending plumes marking the onset of
336 Rayleigh-Taylor instability. Plumes flow from the ALI to the bottom
337 of the flask at a speed of ~1000 µm·min^{-1}. This is in accord with
338 experimental observations. Additionally, plumes serve to transport
339 pyoverdin (over a millimetre scales) and oxygen, which penetrates
340 several millimetres into the liquid phase.

341 **DISCUSSION**

342 The interface between liquid and air defines a niche of significance
343 for many bacteria (4). For aerobic organisms it is an environment
344 replete with oxygen, it offers opportunities for unfettered surface
345 spreading that may aid dispersal and indirectly, may allow rapid
346 colonisation of solid surfaces; colonisation of the ALI may also
347 allow bacteria to escape grazing by solid-surface associated
348 predators. Despite its ecological relevance knowledge of mechanisms
349 and consequences of surface colonisation are poorly understood.
350

351 For more than two decades studies of evolution in experimental
352 microcosms have drawn attention to adaptive mutants of *P. fluorescens*
353 SBW25 that specialise in colonisation of the ALI (22,23,28,33). These
354 mutants, which constitutively overproduce cellulose as a consequence
355 of DGC-activating mutations (24,25,26,29,30,34), reap a significant
356 adaptive advantage in static broth microcosms because of ability to
357 grow at the ALI and thus access to oxygen. Largely unknown however
358 has been the ecological significance of cellulose in the ancestral
359 type and more generally, the role of cellulose in the natural
360 environment. Impeding progress has been the fact that cellulose
361 production is not evident on standard agar plate culture and neither
362 is it produced in shaken broth culture. In the absence of a phenotype
363 *in vitro* it is difficult to make progress.
364

365 Nonetheless, several previous studies have indicated environmental
366 relevance: Gal et al (35) showed a cellulose defective mutant to be
367 significantly less fit than the ancestral type in assays of plant
368 colonisation and Giddens et al (36) showed the cellulose-encoding *wss*
369 operon to be specifically activated on plant root surfaces. Perhaps
370 the most significant finding, but at the time overlooked, was from
371 competitive fitness assays between ancestral SBW25 and a *wss*
372 defective mutant performed in shaken and unshaken microcosms (22): in
373 shaken culture the fitness of the cellulose defective mutant was no
374 different to the ancestral type, but in unshaken culture the mutant
375 was significantly less fit. Here, prompted by recent observation of
376 the poor growth in unshaken culture of SBW25 Δ*wssA-J* (26), combined
377 with new tools of observation, we have come a step closer to
378 understanding the biological significance of bacterial cellulose
379 production.
380
381 Apparent from use of the device shown in Figure 1 is that ancestral
382 SBW25 activates cellulose production in static broth culture and that
383 polymer production allows cells to break through the meniscus and
384 remarkably, grow as micro-colonies on the surface. In the absence of
385 cellulose production, cells are unable to penetrate the ALI and fail
386 to reap the growth advantage that comes from a plentiful supply of
387 oxygen (Fig. 2). Just how cellulose enables bacteria to break through
388 the ALI is unclear. One possibility is that the polymer changes
389 viscosity and this alone is sufficient to propel bacteria through the

390 meniscus, another possibility is that the polymer alters surface
391 charge and that altered electrostatic properties of the cells affects
392 interactions with the surface.
393
394 Also unknown is the signal(s) that lead(s) to activation of cellulose
395 production. What is clear is that known DGC-encoding pathways are
396 necessary to transduce effects through to cellulose production. The
397 fact that three pathways all contribute to differing extents points
398 to complexity in the mapping between DGCs and the cellulosic target
399 (37). It is tempting to suggest that the signal is oxygen, but this
400 seems unlikely because it is incompatible with the previous finding
401 that SBW25 and a cellulose defective mutant are equally fit in an
402 oxygen-replete environment (22). Our suspicion is that the signal
403 stems from some physical attribute of the ALI, possibly surface
404 tension and Marangoni forces arising as a consequence of evaporation
405 or production of surfactant – a subject that received momentary
406 attention almost a century ago (38-40).
407
408 The ecological significance of the behaviour is unknown. Assuming
409 our observations are relevant to the natural environment and not just
410 to laboratory culture, then one possibility is that cells use
411 cellulose to colonise the ALI of water films on plant roots / leaves
412 (the natural environment of SBW25 (41)) and use this environment to
413 aid rapid and unimpeded dispersal. An additional benefit may then
414 accrue on drying when the widely dispersed bacteria are bought back

415 in contact with a solid substrate. Suggestive though that the
416 remarkable growth extending up and out of the liquid surface may hint
417 at a more complex and as yet unrecognised behaviour is the
418 involvement of three DGC-encoding pathways. Why involve three
419 pathways to regulate cellulose production when one would seem to
420 suffice?
421
422 As colonisation of the surface begins to saturate, the heavier
423 material on top becomes unstable and collapses in plumes typical of
424 Rayleigh-Taylor instability. That such behaviour occurs is consistent
425 with the thesis that cellulose is produced just at the meniscus and
426 is not evenly distributed throughout the broth phase. Numerous
427 consequences arise from the ensuing bioconvection, one of which is
428 the rapid transport of water-soluble products. Our particular
429 attention has been the fluorescent molecule pyoverdin, which by
430 virtue of association with cells, is rapidly mixed from the point of
431 production (the ALI) through the entire broth phase of the microcosm.
432 Bioconvection additionally alters the chemical status of the
433 environment, not only through mixing of extant products, but also
434 through effects wrought by enhanced transport of oxygen.
435
436 Transport of pyoverdin has particular significance in light of a
437 previous analysis of SBW25 populations propagated in static KB
438 culture of an extended period (21,42). Common mutant types that rose
439 to prominence harboured mutations that abolished pyoverdin

440 production. The evolutionary advantage of these mutants stemmed not
441 from scavenging of pyoverdin (akin to "cheating"), but from avoidance
442 of the cost of producing pyoverdin when it was not required (21).
443 That pyoverdin is not required in the broth phase (because lack of
444 oxygen means iron exists in the soluble ferrous state) is evident
445 from the time-lapse movies (supplementary movie 7) where pyoverdin
446 production is initiated exclusively at the ALI. However upon reaching
447 the point of Rayleigh-Taylor instability, bioconvection due to
448 cellulose rapidly transports pyoverdin into the broth phase where, in
449 complex with iron, it serves to positively activate transcription of
450 pyoverdin synthetic genes (43)– even though pyoverdin is not required
451 by broth-colonising cells.
452
453 Imaging of cultures as reported here draws attention to the
454 complexity and interdependence of biological, chemical and physical
455 processes. A primary goal of the modelling exercise was to see just
456 how far physical descriptions of measured phenomena such as plume
457 velocity, bacterial density and pyoverdin concentration could account
458 for observed dynamics. Similar approaches have been taken previously
459 in analysis of microbial systems (44,45). Specifically, the model
460 shows how dynamical processes occurring in the liquid can be affected
461 by biofilm formation at the ALI. It also reveals how proliferation
462 of biomass affects the production and transport of pyoverdin.
463 Additionally it accounts for physical transport of water-soluble

464 products and the relative contributions of diffusion versus
465 bioconvection to this process.
466
467 The model generates results consistent with cellulose production at
468 the ALI being sufficient to generate Rayleigh-Taylor instability and
469 initiate fluid movement. The specific mechanisms in the model
470 involve the imbalance between the force of mass repartition in the
471 fluid and the damping force of viscosity. The model also supports
472 hypotheses concerning the critical role of cellulose in
473 bioconvection: numerical resolution of the model showed plumes to
474 have a velocity of ~1000 $\mu m.min^{-1}$ as observed in the experiment.
475 Integrity of plumes – often tens of millimetres in length – is also
476 explained by the model, and arises from the fact diffusion is a minor
477 contributor to fluid dynamics relative to the effects of
478 bioconvection. A further insight concerns ability of bioconvection to
479 mix oxygen into the top few millimetres of the broth phase at a rate
480 that is greater than its consumption. All these effects follow from
481 the Rayleigh-Taylor instability wrought by the production of
482 cellulose at the meniscus.
483
484 Together this study has shed new light on colonisation of the ALI and
485 particularly the role of cellulose — a widespread microbial product
486 (46). Previous work has drawn attention to cellulose as an adhesive
487 substance affecting the relationship between bacteria and solid
488 surfaces (47-50), but these findings stem from study systems that do

489 not provide opportunity for ALI colonisation and perhaps by design
490 even select mutants that over-express cellulose and thus mislead as
491 to ecological significance. This stated, cellulose may play different
492 ecological roles in different organisms and under different
493 conditions. Nonetheless, recognition that production of a polymer
494 can modify an environment thus significantly changing the
495 relationship between the organism and its environment – and the
496 environment in a more general sense – has implications for
497 understanding environments and processes affected by ALI biofilms,
498 such as those encountered in sewage treatment plants, marine and
499 fresh water systems, and in terrestrial environments where transient
500 films of moisture exist in soil pores and on plant surfaces. It also
501 raises intriguing possibilities for future research on the importance
502 of surface tension as a cue eliciting phenotypic responses in
503 bacteria.

504 **MATERIALS AND METHODS**

505 **Bacterial strain and growth conditions.** The ancestral strain of *P.*
506 *fluorescens* SBW25 was isolated from the leaf of a sugar beet plant at
507 the University of Oxford farm (Wytham, Oxford, U.K.; Silby et al.
508 2009). The Δ*wssA-J* strain is deleted of the entire *wssA-J* operon
509 (PFLU0300-PFLU0309) in the ancestral background and comes from (26).
510 The Δ*wsp*, Δ*aws* and Δ*mws* were previously constructed by a two-step
511 allelic exchange strategy (25).

512

513 Strains are cultured in King's Medium B (KB) (51) at 28°C. KB
514 contains (per litre) 20 g bacto™ proteose peptone No. 3 (BD
515 ref211693), 10 g glycerol, 1.5 g K2HPO4 and 1.5 g MgSO4·7H2O.

516

517 To follow bacterial dynamics in experimental flasks bacteria were
518 pre-cultured in KB overnight, centrifuged (6000rpm, 4min) and
519 resuspended in fresh KB. The OD of suspended cultures was adjusted to
520 an OD600nm of 0.8 and stored in 20µl aliquots containing 10µL of
521 cultures of OD 0.8 and 10µL of 60w% autoclaved glycerol. The aliquots
522 were conserved at -80°C.

523

524 To establish each experiment, a rectangular flask (Easy Flask 25cm²
525 Nunc) was filled with 20ml of KB medium. A 20µl -80°C cultlure was
526 then defrosted and inoculated in the KB at a final dilution of 10^4
527 $cfu.ml^{-1}$. The flask was positioned in the setup shown in Figure 1 and
528 incubated at 28°C in an IGS60 HERATHERM static incubator.

529

530 **Experimental setup to measure the dynamics of unshaken bacterial**
531 **culture.** The setup was designed and built to perform custom
532 measurements and details are available from the authors upon request.
533 The device comprises a laser-photodiode alignment to measure optical
534 density in the flask and three cameras to observe the ALI as well as
535 the biomass and the pyoverdin in the liquid phase.

536

537 To measure the optical density of the liquid phase a vertical profile
538 was obtained by scanning with a laser-photodiode detector mounted on
539 a lifter. A plastic piece that was produced by a 3D-printer on a
540 stratasys fortus250 in ABS (yellow on Fig. 1) joined the laser-
541 photodiode to a carriage that was free to slide on a vertical rail
542 (ingus TS-01-15/TW-01-15) driven by a M10 cage bolt coupled to a M10
543 threaded rod. This ensured a precise vertical and horizontal
544 positioning of the laser-photodiode alignment. The thread rode was
545 smoothly rotated using a 7,2Vcc motor. A L293D power switch
546 controlled by an Arduino board MEGA 2560 directed rotation of the
547 motor. The thread rod rotation angle was measured with an optical
548 encoder HEDS5500 500CPR. Ultimately, this allowed measurement of the
549 vertical position of the laser beam with a resolution of ~3µm.

550

551 The photodiode was from Thorlabs (FDS1010), the laser a HLM1230 of
552 wavelength 650 nm and power 5mW. To ensure that the laser did not
553 harm bacteria the light was attenuated by a NE520B (Thorlabs) neutral

554 density filter of OD=2. The optical density of the culture was
555 evaluated by measuring the photo-current produced by the laser
556 hitting the photodiode after it went through the flask. To ensure
557 linearity between the intensity of light hitting the photodiode and
558 its conversion in photo-current, the photodiode was polarised in
559 inverse with 5V provided by a LM4040 electronic component. The photo-
560 current was estimated by measuring the voltage of a 437 ± 5% kΩ
561 resistor mounted in serial with the photodiode. The voltage was
562 monitored by the Arduino MEGA 2560 board encoding a 0-5V analogic
563 input on 10 bits giving a resolution of 5mV. After subsequent
564 calibration, the signal acquired by the system allowed estimation of
565 the bacterial concentration in the flask within a range of 10^7-$5 \cdot 10^9$
566 bact·ml^{-1}.
567
568 Synchronized with the laser-photodiode, were three cameras: a uEyeLE
569 USB2.0 Camera, a 1/2" CMOS Monochrome Sensor, and a 1280x1024 Pixel
570 equipped with a CMFA0420ND 4 mm ½ inch lens. The first camera (Fig.
571 1) records a bright field image of the vertical side view of the
572 culture medium. The second camera is equipped with a band pass
573 optical filter 470 ± 10nm (Thorlabs FB470-10). It takes a side view
574 of the culture medium. During its acquisition a 405nm laser (405MD-5-
575 10-1235) illuminates the flask to excite pyoverdin fluorescence. The
576 third camera takes a bright field image of the ALI with an angle of
577 ~45°. Acquisition of optical density data and photos were
578 synchronized using a master script written in Python that recorded

579 the data produced by the Arduino board and saved the photos taken by
580 the cameras.
581
582 **Colonization of the air-liquid interface ALI (Fig. 4).** To observe the
583 effect of Δ*wsp*, Δ*aws* and Δ*mws* mutations on ALI colonization, we use
584 6-well plates Greiner bio-one 657160 filled with 8ml of KB. Each well
585 was inoculated from glycerol stocks. The 6-well plates ere incubated
586 at 28°C without shaking. Pictures were taken the ALI with a Nikon
587 D7000 camera equipped with an AF-S DX NIKKOR 18-105mm f/3.5-5.6G ED
588 VR objective.
589
590 **The Model.** The model uses six fields to describe the system: the
591 vector field of the fluid vorticity (ω), the scalar field of the
592 fluid stream function (Ψ) and the scalar fields of bacterial (b),
593 oxygen (o), cellulose (c) and pyoverdin (p) concentrations. We also
594 use a derived vector field that represents the velocity of the fluid
595 (u). The model is valid for a three dimensional space but we estimate
596 its validity in a two dimensional space in order to reduce the time
597 of numerical computation. That is why we choose a fluid description
598 in term of vorticity (ω) and the stream function (Ψ). This
599 description gives two advantages for the numerical resolution of the
600 model. First, the equation of the fluid incompressibility is solved
601 by construction; second, the calculation of the vorticity vector can

be reduced to the calculation of a simple scalar field (for more detail see (35)).

With the six fields given above come six partial differential equations that describe their dynamics.

The first equations related to the stream function. This scalar field is calculated by a Poisson equation:

Equation 1

$$\Delta\Psi = -\omega$$

Where, Δ is the Laplace operator.

The second equation deals with the vorticity reduced to a simple scalar field. Its dynamics can be derived from the Navier-Stokes (NS) equation:

Equation 2

$$\frac{\partial\omega}{\partial t} + (\vec{u} \bullet \vec{\nabla})\omega = \nu\Delta\omega - g\frac{\partial}{\partial x}\left(\frac{\rho}{\rho_0}\right)$$

The left side of NS is the Lagrangian derivative of the vorticity. The right side contains damping of the vorticity by the viscosity ν, and a gravity term traduces the generation of vorticity due to the uneven spatial repartition of the mass density ρ relative to the density of the fluid medium ρ_0. The operator $(\vec{u} \bullet \vec{\nabla})$ stem for the convective derivative. In the equation, the local mass density ρ takes into account the mass density of the liquid medium ρ_0, bacteria ρ_b and cellulose ρ_c. Hence we consider the local mass density (ρ) as

the sum of the mass contribution of the liquid medium, the bacteria and the cellulose. Explicitly the notation ρ *stem for*:

$$\rho = \rho_0 + \Phi_b(\rho_b - \rho_0) + \Phi_c(\rho_c - \rho_0)$$

where Φ_b is the local volume fraction of the bacteria and Φ_b the local volume fraction of the cellulose.

To calculate the dynamics of the concentration of bacteria (b), cellulose (c) and pyoverdin (p), we write a diffusion-reaction-convection equation.

To write the third equation dealing with bacteria we make several assumptions:

Equation 3

$$\frac{\partial \mathrm{b}}{\partial t} + (\vec{u} \bullet \vec{\nabla})b = D_b \Delta b + \delta b \left(1 - \frac{b}{b_{sat}}\right)$$

bacteria grow exponentially until they reach the saturation b_{sat} measured experimentally (Fig. 2) and, bacteria consume oxygen that is dissolved into the liquid.

The left-hand side of the bacterial equation is the Lagrangian derivative applied to b. The right-hand side contains a diffusive term that takes into account the random motility of bacteria with a diffusion coefficient D_b, and an exponential growth term with a rate δ that goes to zero when the concentration reach the b_{sat} value.

The fourth equation describes the dynamics of the oxygen (o) field. Bacteria consume the oxygen at a rate γ.

Equation 4

$$\frac{\partial \mathrm{o}}{\partial t} + \left(\vec{u} \bullet \vec{\nabla}\right) o = D_o \Delta o - \gamma b\, \Theta(o)$$

The coefficient of diffusion is D_o. Oxygen consumption goes to zero when there is no more oxygen. This is ensure that multiplying the consumption term by the Heaviside function ($\Theta(o)$) is 1 when o is above zero, but zero otherwise.

The fifth equation assumes that the cellulose is produced with an exponential rate (α) as long as the oxygen concentration is higher than o^* and the concentration of bacteria is higher than b^*. Additionally, cellulose production saturates when c tends to 1, its maximal value. The equation is:

Equation 5

$$\frac{\partial \mathrm{c}}{\partial t} + \left(\vec{u} \bullet \vec{\nabla}\right) c = D_c \Delta c + \alpha c(1-c)\Theta(b-b^*)\, \Theta(o-o^*)$$

The sixth equation describes the dynamics of pyoverdin production. Provided that the local concentration of oxygen is sufficiently high bacteria produce pyoverdin according to the autocatalytic synthesis measured experimentally (Fig. 5D) with a rate β. The equation is:

Equation 6

$$\frac{\partial \mathrm{p}}{\partial t} + \left(\vec{u} \bullet \vec{\nabla}\right) p = D_p \Delta p + \beta p(1-p)\, \Theta(o-o^*)$$

Here, pyoverdin production goes to zero when oxygen concentration is below o^* by multiplying the production term by a Heaviside function $\Theta(o-o^*)$.

Finally, to calculate the fluid velocity we use the derivative of the stream function where u_x and u_y stand for the horizontal and vertical components of the fluid velocity (u):

$$u_x = \frac{\partial \Psi}{\partial y}$$

$$u_y = -\frac{\partial \Psi}{\partial x}$$

Numerical Simulations. We used a finite difference method to solve the coupled reaction-diffusion-convection equations (35). The simulation was performed on a Linux system: Debian 4.9.51-1, gcc 6.3.0. The hardware CPU was an Intel(R)Core(TM) i7-7700K @ 4.2Ghz with 16GB RAM. The parameters used in the simulation displayed Figure 7 are listed in Table 1.

ACKNOWLEDGEMENTS

We thank Nicolas Desprat, Clara Moreno Fenoll, Steven Quistad and Guilhem Doulcier for discussion and comment. MA was supported by HFSP grant RGP0010/2015.

686 **REFERENCES**

687 1. Costerton JW, Stewart PS, Greenberg EP. 1999. Bacterial
688 biofilms: a common cause of persistent infections. Science
689 284:1318-22.
690 2. Davey ME, O'Toole G A. 2000. Microbial biofilms: from ecology
691 to molecular genetics. Microbiol Mol Biol Rev 64:847-67
692 3. Flemming HC, Wingender J, Szewzyk U, Steinberg P, Rice SA,
693 Kjelleberg S. 2016. Biofilms: an emergent form of bacterial
694 life. Nat Rev Microbiol 14:563-75.
695 4. Marshall, K. C. 1996. *Adhesion as a strategy for access to*
696 *nutrients* (pp. 59-87). Wiley: New York.
697 5. Watnick P, Kolter R. 2000. Biofilm, city of microbes. J
698 Bacteriol 182:2675-9.
699 6. Donlan RM. 2002. Biofilms: microbial life on surfaces.
700 Emerging infectious diseases 8:881-890.
701 7. Alsharif G, Ahmad S, Islam MS, Shah R, Busby SJ, Krachler AM.
702 2015. Host attachment and fluid shear are integrated into a
703 mechanical signal regulating virulence in *Escherichia coli*
704 O157: H7. Proc Natl Acad Sci U.S.A. 102:5503-5508.
705 8. Stewart PS. 2002. Mechanisms of antibiotic resistance in
706 bacterial biofilms. Int J Med Microbiol 292:107-13.
707 9. Dang H, Lovell CR. 2016. Microbial surface colonization and
708 biofilm development in marine environments. Microbiol Mol
709 Biol Rev 80:91-138.
710 10. Hamilton WD, May RM. 1977. Dispersal in stable habitats.

711 Nature 269:578-581.
712 11. Monds RD, O'Toole GA. 2009. The developmental model of
713 microbial biofilms: ten years of a paradigm up for review.
714 Trends Microbiol 17:73-87.
715 12. O'Toole GA, Wong GC. 2016. Sensational biofilms: surface
716 sensing in bacteria. Curr Opin Microbiol 30:139-146.
717 13. Heydorn A, Nielsen AT, Hentzer M, Sternberg C, Givskov M,
718 Ersboll BK, Molin S. 2000. Quantification of biofilm
719 structures by the novel computer program COMSTAT. Microbiol
720 146:2395-407.
721 14. Azeredo J, Azevedo NF, Briandet R, Cerca N, Coenye T, Costa
722 AR, Desvaux M, Di Bonaventura G, Hébraud M, Jaglic Z. 2017.
723 Critical review on biofilm methods. Crit Rev Microbiol
724 43:313-351.
725 15. Petrova OE, Sauer K. 2012. Sticky situations: key components
726 that control bacterial surface attachment. J Bacteriol
727 194:2413-2425.
728 16. Valentini M, Filloux A. 2016. Biofilms and cyclic di-GMP (c-
729 di-GMP) signaling: Lessons from *Pseudomonas aeruginosa* and
730 other bacteria. J Biol Chem 291:12547-55.
731 17. Kjelleberg, S. (1985). Mechanisms of bacterial adhesion at
732 gas-liquid interfaces. In *Bacterial Adhesion* (pp. 163-194).
733 Springer, Boston, MA.
734 18. Wotton RS, Preston TM. 2005. Surface films: Areas of water
735 bodies that are often overlooked. AIBS Bull. 55:137-145.

736 19. Neilands JB. 1981. Microbial iron compounds. Annu Rev
737 Biochem 50:715-31.
738 20. Koza A, Moshynets O, Otten W, Spiers AJ. 2011. Environmental
739 modification and niche construction: developing O2 gradients
740 drive the evolution of the Wrinkly Spreader. ISME J 5:665-73.
741 21. Zhang XX, Rainey PB. 2013. Exploring the sociobiology of
742 pyoverdin-producing *Pseudomonas*. Evolution 67:3161-74.
743 22. Spiers AJ, Kahn SG, Bohannon J, Travisano M, Rainey PB.
744 2002. Adaptive divergence in experimental populations of
745 *Pseudomonas fluorescens*. I. Genetic and phenotypic bases of
746 wrinkly spreader fitness. Genetics 161:33-46.
747 23. Rainey PB, Rainey K. 2003. Evolution of cooperation and
748 conflict in experimental bacterial populations. Nature
749 425:72.
750 24. Bantinaki E, Kassen R, Knight C, Robinson Z, Spiers A,
751 Rainey P. 2007. Adaptive divergence in experimental
752 populations of Pseudomonas fluorescens. III. Mutational
753 origins of wrinkly spreader diversity. Genetics 176:441-453.
754 25. McDonald MJ, Gehrig SM, Meintjes PL, Zhang X-X, Rainey PB.
755 2009. Adaptive divergence in experimental populations of
756 *Pseudomonas fluorescens*. IV. Genetic constraints guide
757 evolutionary trajectories in a parallel adaptive radiation.
758 Genetics. 161: 33-46.
759 26. Lind PA, Farr AD, Rainey PB. 2017. Evolutionary convergence
760 in experimental *Pseudomonas* populations. ISME J 11:589.

761 27. Plesset MS, Whipple CG, Winet H. 1976. Rayleigh-Taylor
762 instability of surface layers as the mechanism for
763 bioconvection in cell cultures. J Theor Biol 59:331-351.
764 28. Rainey PB, Travisano M. 1998. Adaptive radiation in a
765 heterogeneous environment. Nature 394:69-72.
766 29. Lind PA, Farr AD, Rainey PB. 2015. Experimental evolution
767 reveals hidden diversity in evolutionary pathways. eLife
768 4:e07074.
769 30. Lind PA, Libby E, Herzog J, Rainey PB. 2019. Predicting
770 mutational routes to new adaptive phenotypes. eLife 8:e38822.
771 31. Visca P, Imperi F, Lamont IL. 2007. Pyoverdine siderophores:
772 from biogenesis to biosignificance. Trends Microbiol 15:22-
773 30.
774 32. Pozrikidis C. 2016. *Fluid Dynamics: Theory,Ccomputation, And*
775 *Numerical Simulation*. Springer.
776 33. Spiers AJ, Bohannon J, Gehrig SM, Rainey PB. 2003. Biofilm
777 formation at the air–liquid interface by the *Pseudomonas*
778 *fluorescens* SBW25 wrinkly spreader requires an acetylated
779 form of cellulose. Mol Microbiol 50:15-27.
780 34. Goymer P, Kahn S, Malone J, Gehrig S, Spiers A, Rainey P.
781 2006. Adaptive divergence in experimental populations of
782 *Pseudomonas fluorescens*. II. The role of the GGDEF regulator
783 WspR in evolution and development of the wrinkly spreader
784 phenotype. Genetics. 161:33-46.
785 35. Gal M, Preston GM, Massey RC, Spiers AJ, Rainey PB. 2003.

786 Genes encoding a cellulosic polymer contribute toward the
787 ecological success of *Pseudomonas fluorescens* SBW25 on plant
788 surfaces. Mol Ecol 12:3109-3121.
789 36. Giddens SR, Jackson RW, Moon CD, Jacobs MA, Zhang X-X,
790 Gehrig SM, Rainey PB. 2007. Mutational activation of niche-
791 specific genes provides insight into regulatory networks and
792 bacterial function in a complex environment. Proc Natl Acad
793 Sci U.S.A. 104(46):18247-18252.
794 37. Yan J, Deforet M, Boyle KE, Rahman R, Liang R, Okegbe C,
795 Dietrich LE, Qiu W, Xavier JB. 2017. Bow-tie signaling in c-
796 di-GMP: Machine learning in a simple biochemical network.
797 PLoS Comp Biol 13:e1005677.
798 38. Frobisher Jr M. 1926. Relations of surface tension to
799 bacterial phenomena. J Infect Dis 38:66-91.
800 39. Gibbs WM, Batchelor H, Sickels T. 1926. Surface tension and
801 bacterial growth. J Bacteriol 11:393.
802 40. Pizarro OR. 1927. The relation of surface tension to
803 bacterial development. J Bacteriol 13:387.
804 41. Rainey PB, Bailey MJ. 1996. Physical and genetic map of the
805 *Pseudomonas fluorescens* SBW25 chromosome. Mol Microbiol
806 19:521-533.
807 42. Rainey PB, Desprat N, Driscoll WW, Zhang XX. 2014. Microbes
808 are not bound by sociobiology: Response to Kümmerli and Ross-
809 Gillespie (2013). Evolution 68:3344-3355.
810 43. Lamont IL, Beare PA, Ochsner U, Vasil AI, Vasil ML. 2002.

811 Siderophore-mediated signaling regulates virulence factor
812 production in *Pseudomonas aeruginosa*. Proc Natl Acad Sci
813 U.S.A. 99:7072-7077.
814 44. Ardré M, Henry H, Douarche C, Plapp M. 2015. An individual-
815 based model for biofilm formation at liquid surfaces. Phys
816 Biol 12:066015.
817 45. Tuval I, Cisneros L, Dombrowski C, Wolgemuth CW, Kessler JO,
818 Goldstein RE. 2005. Bacterial swimming and oxygen transport
819 near contact lines. Proc Natl Acad Sci U.S.A. 102:2277-2282.
820 46. Ross P, Mayer R, Benziman M. 1991. Cellulose biosynthesis
821 and function in bacteria. Microbiol Mol Biol Rev 55:35-58.
822 47. Matthysse A. 1983. Role of bacterial cellulose fibrils in
823 *Agrobacterium tumefaciens* infection. J Bacteriol 154:906-915.
824 48. Da Re S, Ghigo J-M. 2006. A CsgD-independent pathway for
825 cellulose production and biofilm formation in *Escherichia*
826 *coli*. J Bacteriol 188:3073-3087.
827 49. Serra DO, Richter AM, Hengge R. 2013. Cellulose as an
828 architectural element in spatially structured *Escherichia*
829 *coli* biofilms. J Bacteriol 195:5540–5554.
830 50. Zogaj X, Nimtz M, Rohde M, Bokranz W, Römling U. 2001. The
831 multicellular morphotypes of *Salmonella typhimurium* and
832 *Escherichia coli* produce cellulose as the second component of
833 the extracellular matrix. Mol Microbiol 39:1452-1463.
834 51. King EO, Ward MK, Raney DE. 1954. Two simple media for the
835 demonstration of pyocyanin and fluorescin. Transl Res 44:301-

836 307.
837 52. Flemming HC, Wingender J. 2010. The biofilm matrix. Nat Rev
838 Microbiol 8:623.
839 53. Bratbak G, Dundas I. 1984. Bacterial dry matter content and
840 biomass estimations. App Env Microbiol 48:755-757.
841 54. Berg HC. 1993. *Random Walks in Biology*. Princeton University
842 Press.
843 55. Krieger IM, Mulholland GW, Dickey CS. 1967. Diffusion
844 coefficients for gases in liquids from the rates of solution
845 of small gas bubbles. J Phys Chem 71:1123-1129.
846 56. Martí S, Rodríguez-Baño J, Catel-Ferreira M, Jouenne T, Vila
847 J, Seifert H, Dé E. 2011. Biofilm formation at the solid-
848 liquid and air-liquid interfaces by *Acinetobacter* species.
849 BMC Res Notes 4:5.
850

851 **FIGURES**

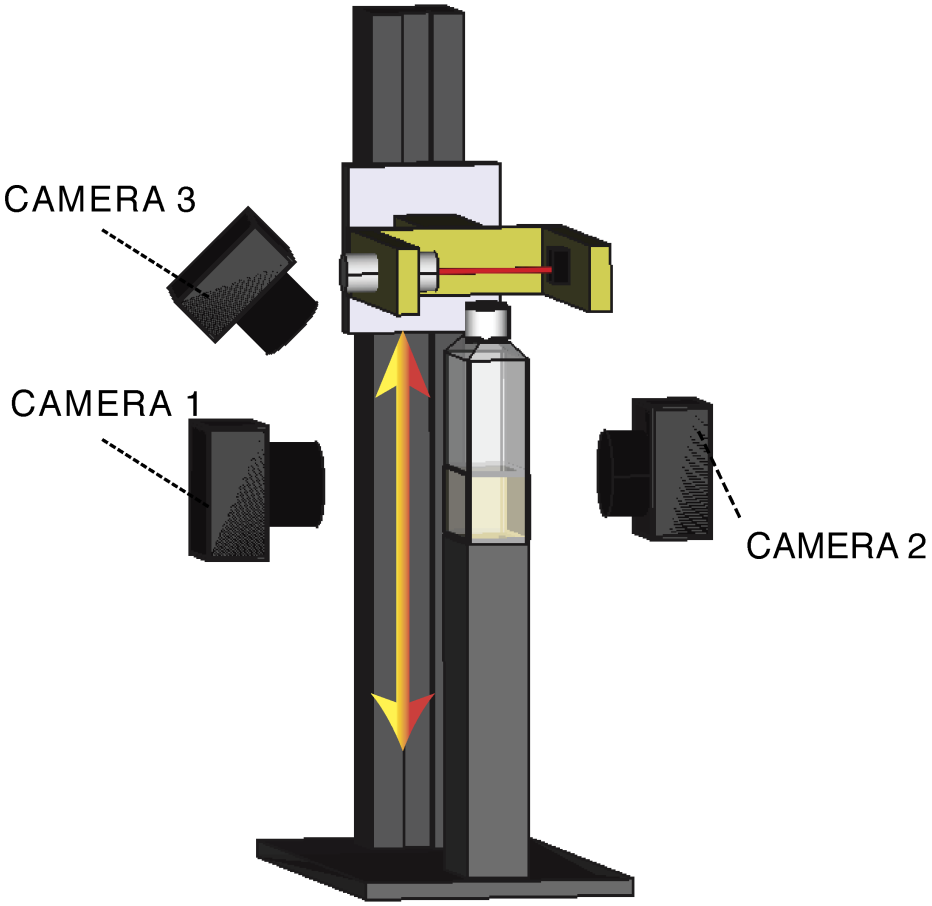

852

853 **FIG 1** Experimental device. A polycarbonate cell-culture bottle
854 filled with 20 ml of King's Medium B and inoculated with bacteria is
855 placed on a fixed vertical stand. The device and associated cameras
856 are maintained within a 28°C incubator. The flask is scanned
857 vertically every 5min with a 600 nm laser beam with 1mm section.
858 Light passing through the flask is collected by a photodiode. To
859 obtain a measure of the optical density in the flask along a vertical
860 profile, the alignment laser-photodiode is coupled to a motorised
861 device that ensures smooth vertical translation. Three cameras are
862 located around the flask. The first (camera 1) obtains a side-view

863 image of the liquid phase of the medium using bright-field
864 illumination. The second (camera 2), also fixed perpendicular to the
865 flask, monitors fluorescence associated with pyoverdin (excitation
866 405/emission 450nm). The third camera (camera 3) is oriented with a
867 45° angle and captures growth at the ALI using bright-field
868 illumination.
869

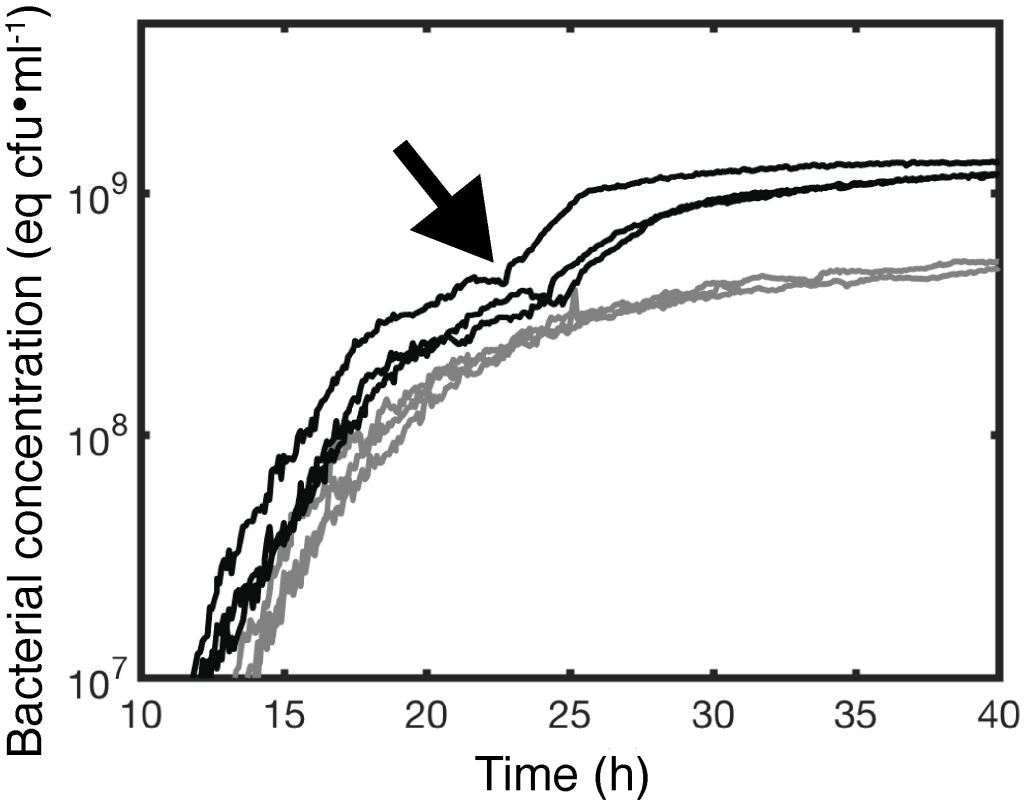

870

871 **FIG 2** Production of cellulose maximises growth in static broth
872 culture. Dynamics of growth of *P. fluorescens* SBW25 (black lines)
873 and *P. fluorescens* SBW25 Δ*wssA-J* (cellulose negative mutant) (grey
874 lines) in unshaken King's Medium B as determined by the scanning
875 laser device and associated photodiode depicted in Figure 1. Data are
876 average optical density at 600 nm (OD_{600}) obtained from scanning the
877 vertical section of three independent flasks at 5 min intervals. OD_{600}
878 measures are calibrated using direct plate counts of colony forming
879 units (equivalent cfu·ml^{-1}). The arrow denotes the onset of
880 bioconvection caused by production of cellulose that marks a
881 secondary increase in growth. This second growth phase is absent in
882 the cellulose negative mutant.

883

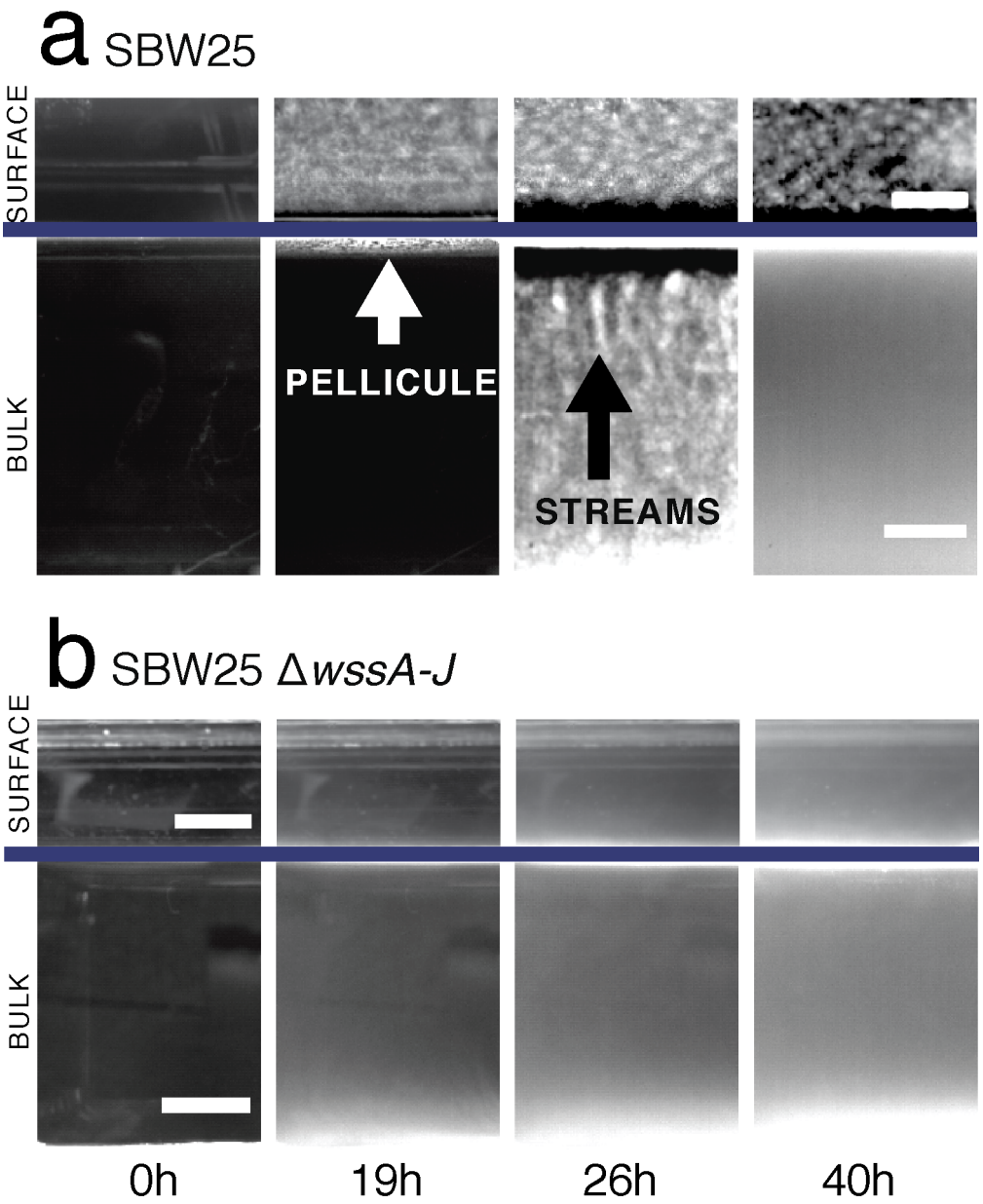

FIG 3 Cellulose is necessary for growth at the air-liquid interface (ALI) and results in bioconvection. Bright-field images of ancestral *P. fluorescens* SBW25 (a) and *P. fluorescens* SBW25 Δ*wssA-J* (cellulose negative mutant) (b) taken at four time intervals. Complete movies are available as SI movie files 1,2,6 and 7. Images above the solid line show growth at the ALI captured using camera 3; images below the line are from camera 1 (see Figure 1). At time 0 h the medium is

892 inoculated with ~10^4 cells·ml^{-1}. By 19h the ancestral cellulose-
893 producing genotype has formed a thin white pellicle at the ALI
894 (visible by both camera 1 and 3). No pellicle formation is seen in
895 the cellulose negative mutant, but growth is evident in the broth
896 phase. By 26 h, in cultures of the cellulose-producing ancestral
897 type, plumes characteristic of bioconvection stream from the ALI. No
898 evidence of mat formation or streaming is seen in SBW25 Δ*wssA-J*. By
899 40h streaming has largely ceased in the ancestral type, although
900 growth is still apparent at the ALI. Scale bars are 5mm. Contrast
901 has been adjusted to highlight salient features.
902

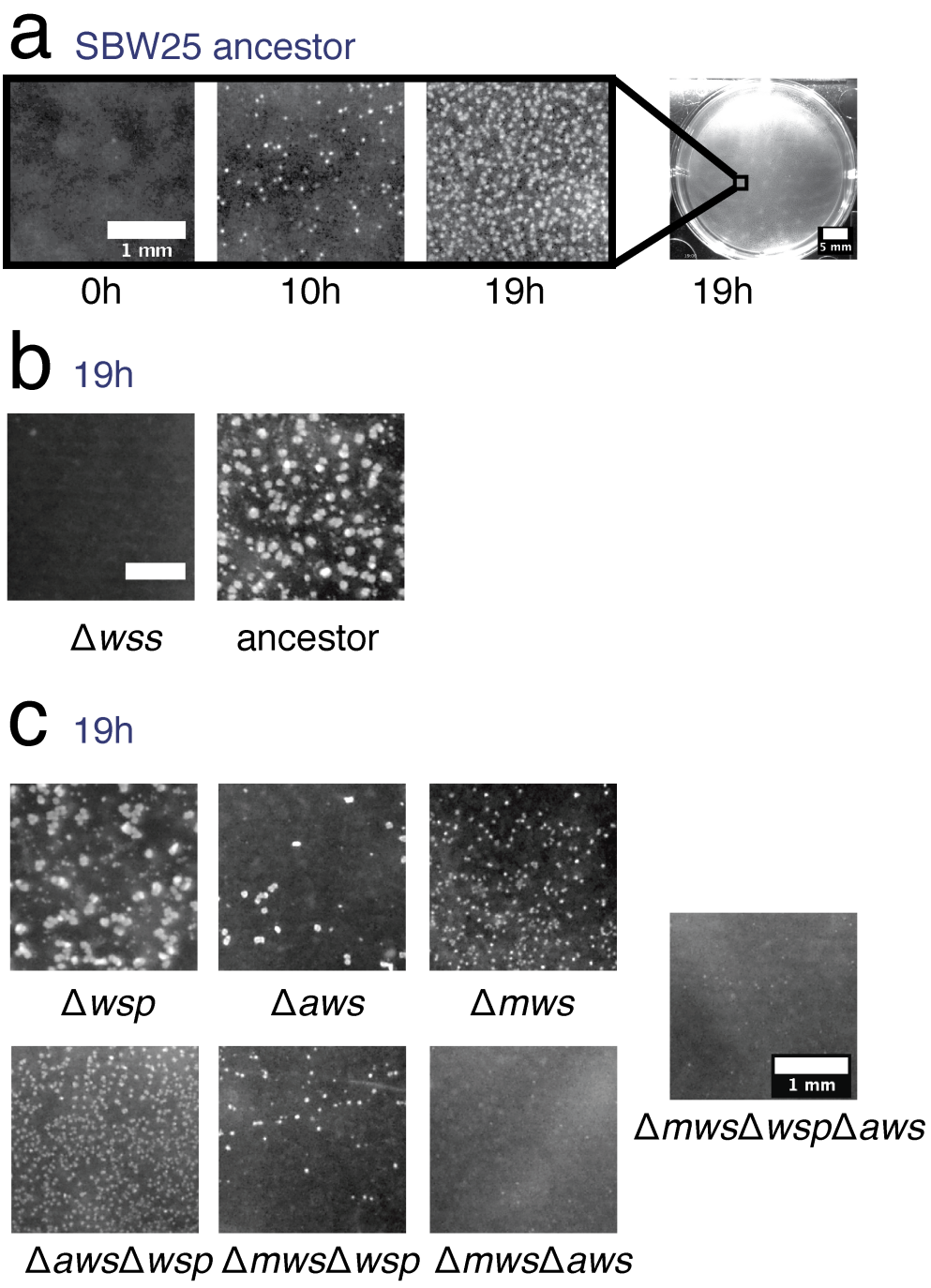

903

904 **FIG 4** Multiple diguanylate cyclase are required for colonisation of
905 the ALI. Micro-colony formation at the ALI for ancestral *P.*
906 *fluorescens* SBW25 and a range of mutants captured from a camera
907 mounted directly above individual wells of a six-well tissue culture
908 plate containing 5 ml King's Medium B. Time course of micro-colony

909 formation for ancestral *P. fluorescens* SBW25 (a). Comparison with
910 SBW25 Δ*wssA-J* (cellulose negative mutant) at 19 h (b). Patterns of
911 micro-colony formation at 19 h in mutants devoid of Wsp (Δ*wsp*), Aws
912 (Δ*aws*) and Mws (Δ*mws*) diguanylate cyclase-encoding pathways and
913 combinations there-of. Scale bar is 1 mm, except for the entire well
914 in (a) which is 5 mm.
915
916

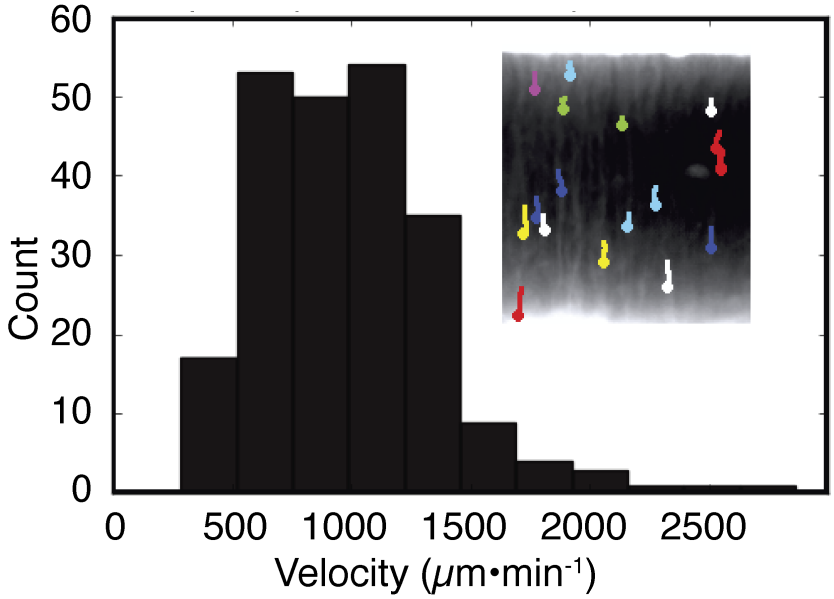

FIG 5 Bioconvection caused by cellulose. Time lapse images via bright field camera 1 (Fig. 1) capture biomass dynamics in the liquid medium. By 25 h Rayleigh-Taylor instability generates plumes of biomass that fall from the ALI to the bottom of the flask (inset). The velocity of movement is obtained by tracking trajectories of the plumes. The frequency distribution of plume velocity reveals a mean speed of 983 ± (SD) 373 $\mu m \cdot min^{-1}$.

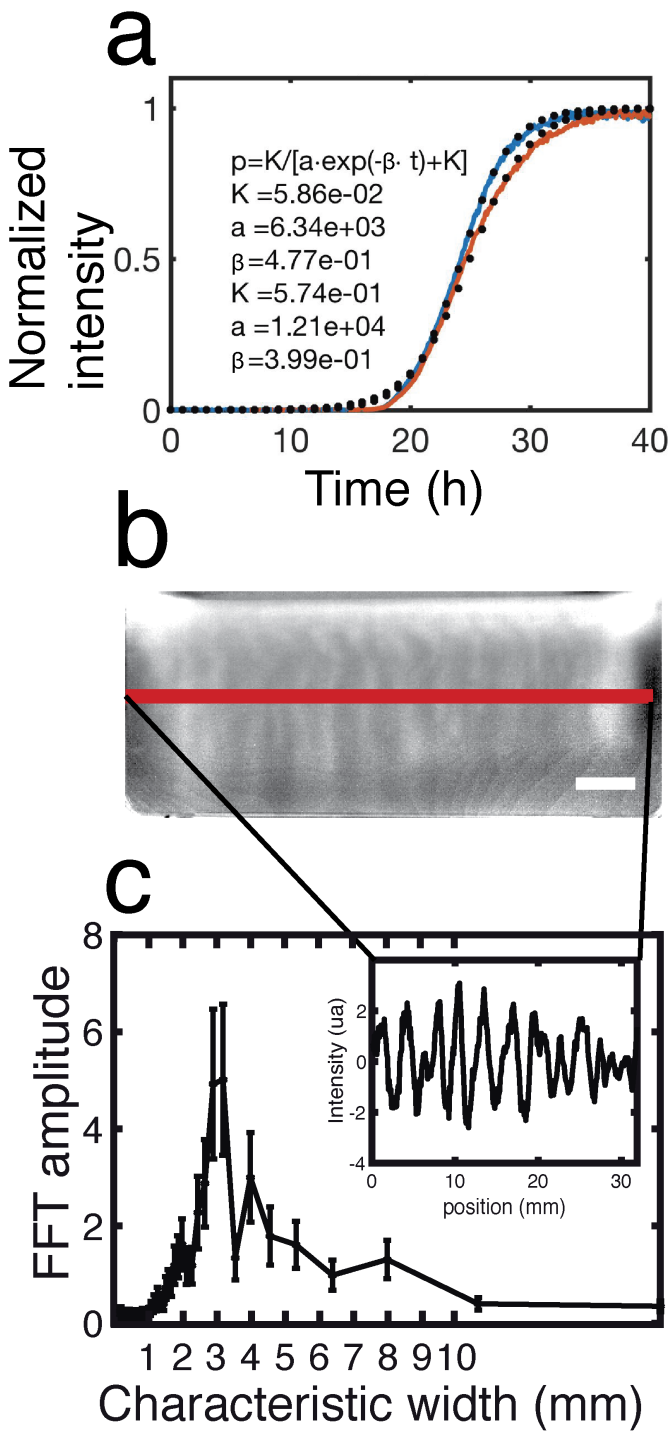

FIG 6 Bioconvection. Camera 2 (see Figure 1) monitors pyoverdin concentration in the flask by measuring fluorescence. Pyoverdin is produced primarily at the ALI. The fluorescence at the position of the ALI increases with time like a sigmoid curve (a). The adhoc logistic function of the inset gives the normalized intensity (*p*) as a function of the time (*t*) and the parameters of the fit (*K*, *a* and

938 β). The fitted curves (dotted line) adjust the experimental curves
939 (plain line) for the estimated values of the parameters given in
940 inset. Plumes due to Rayleigh-Taylor instability transport pyoverdin
941 from the ALI to the liquid phase. Pyoverdin concentration is
942 transiently higher along vertical columns that correspond to the
943 plumes flowing from the ALI. The white scale bar is 5mm. The
944 fluorescence intensity profile along the red horizontal line (b)
945 shows that pyoverdin is distributed with a fluctuating spatial
946 structure (inset). Fast Fourier transformation (FFT) of the intensity
947 profile reveals these fluctuations to have a characteristic
948 wavelength of 3mm.
949

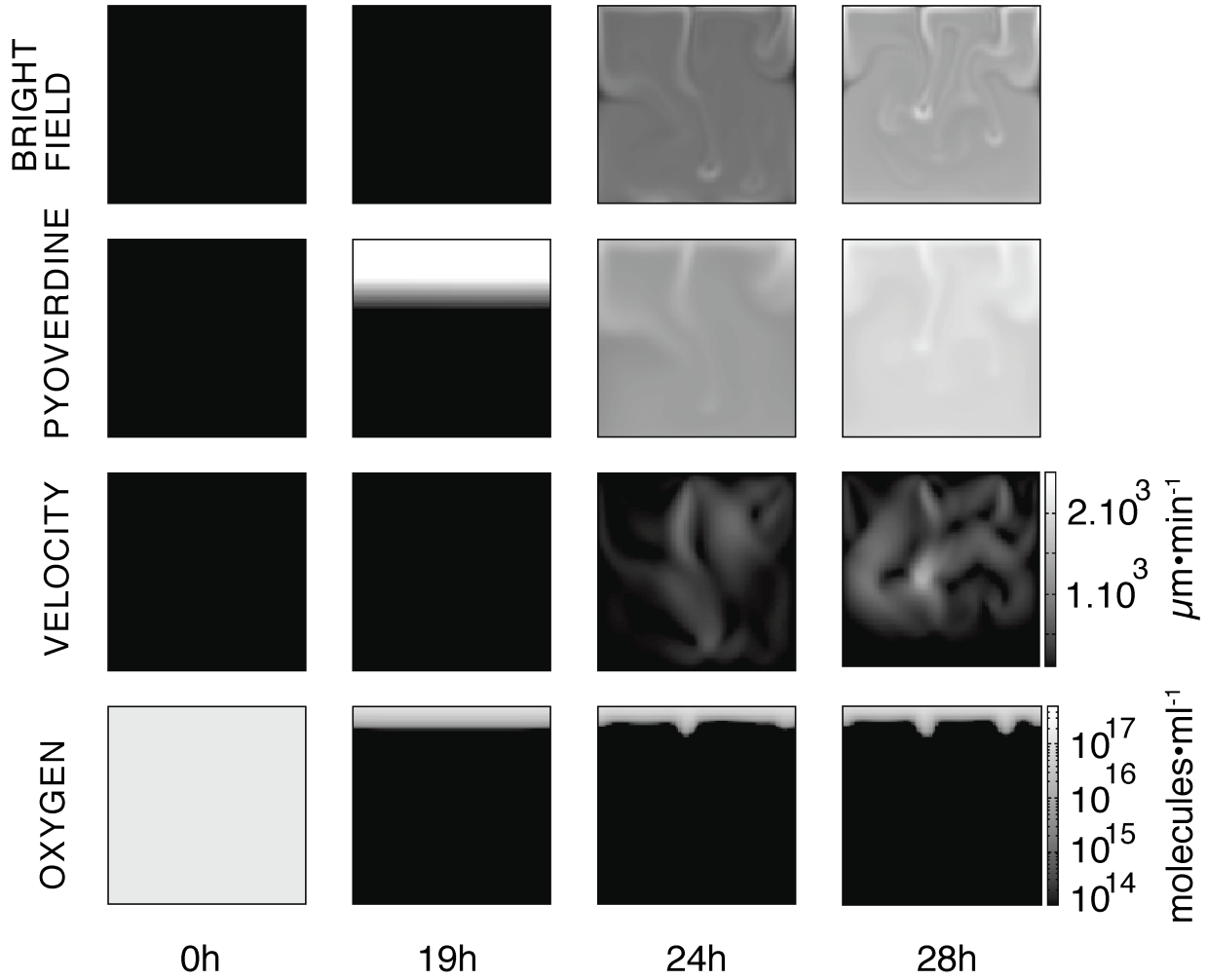

FIG 7 Numerical simulation of the mathematical model. Images display the dynamics of the simulated microcosm from inoculation at 0h to 28h. Time resolved movies are available in supplementary movies 8-11. The first row above shows the dynamics of the biomass in the bulk (bacteria and cellulose) as if observed with bright field illumination 1 (Fig. 1). In experiments, at 24h, plumes concentrated in biomass flow are evident in the liquid phase. The second row shows the concentration of pyoverdin in the liquid phase. The plumes transport pyoverdin into the bulk phase. The third row shows the dynamics of liquid velocity. When bioconvection is activated fluid

961 flow is of the order of 1000 $\mu m \cdot min^{-1}$, which is consistent with the
962 measurements shown (Fig. 5). The fourth row shows the dynamics of
963 oxygen concentration. Soon after inoculation oxygen in the bulk phase
964 is eliminated due to metabolic (oxygen consuming) activities of
965 bacteria. The supply of oxygen at the ALI combined with growth of
966 bacteria and production of cellulose means a gradient of oxygen 2-3
967 mm into the liquid. Images at 24h and 28h show that oxygen transport
968 from the ALI before consumption by bacteria in the liquid phase.
969 The square images are 1 cm^2 and contrast is identical across each
970 row.

971 **TABLE 1.** Parameters, values and sources of data used for the model.

Name	Symbol	Value	Unit	Source
time step	Δt	$1 \cdot 10^{-3}$	s	
spatial step	Δx	$1 \cdot 10^{-4}$	m	
grid size NxN	N	100	pixel	
fluid dynamics viscosity	η	$8.9 \cdot 10^{-4}$	$kg \cdot m \cdot s$	handbook
bacterial volume	V_b	$3 \cdot 10^{-18}$	m^{-3}	experimental evidence
water mass density	ρ_0	$0.995 \cdot 10^{3}$	$kg \cdot m^{-3}$	(52)
bacterial mass density	ρ_b	$1.193 \cdot 10^{3}$	$kg \cdot m^{-3}$	(56)
cellulose mass density	ρ_c	$1.5 \cdot 10^{3}$	$kg \cdot m^{-3}$	
maximal bacterial concentration	b_{sat}	$3 \cdot 10^{14}$	bacteria $\cdot m^{-3}$	experimental fit
initial concentration of bacteria	b_0	$2 \cdot 10^{10}$	bacteria $\cdot m^{-3}$	experimental settings
diffusion coefficient of bacteria	D_b	$1 \cdot 10^{-10}$	$m^2 \cdot s^{-1}$	(57)
diffusion coefficient of cellulose	D_c	$5 \cdot 10^{-11}$	$m^2 \cdot s^{-1}$	adhoc
diffusion coefficient of	D_o	$1 \cdot 10^{-9}$	$m^2 \cdot s^{-1}$	(58)

Name	Symbol	Value	Unit	Source
oxygen				
diffusion coefficient of pyoverdin	D_p	$3 \cdot 10^{-10}$	$m^2 \cdot s^{-1}$	measured
initial oxygen concentration	O_0	$1.5 \cdot 10^{23}$	molecules $\cdot m^{-3}$	(45)
initial pyoverdin concentration	p_0	$3.36 \cdot 10^{-5}$	au	experimental fit
initial cellulose concentration	c_0	$1 \cdot 10^{-8}$	au	adhoc
production of pyoverdin	β	$1.22 \cdot 10^{-4}$	s	experimental fit
production of cellulose	α	$1 \cdot 10^{-3}$	s	adhoc
growth rate bacteria	δ	0.53	h^{-1}	experimental fit
oxygen consumption per bacteria per second	γ	$1 \cdot 10^{6}$	molecules $\cdot$bacteria^{-1} $\cdot s^{-1}$	(45)
volume of cellulose produced per bacteria	$10 \cdot V_b$	$3 \cdot 10^{-17}$	m^3	(55)

Name	Symbol	Value	Unit	Source
minimal bacterial concentration for cellulose production	$b^* = b_{sat}/3$	$1 \cdot 10^{14}$	bacteria $\cdot m^{-3}$	experimental evidence
Boundary condition of oxygen at the top	O_0	$1.5 \cdot 10^{23}$	molecules $\cdot m^{-3}$	(45)
acceleration of gravity	g	9.81	$m \cdot s^{-2}$	
minimal oxygen concentration for cellulose and pyoverdin production	o^*	$O_0 \cdot 10^{-1}$	molecules $\cdot m^{-3}$	adhoc

976 **SUPPLEMENTARY FILES**

977 Supplementary movie file 1.

978 Name of file: supplementaryMovie1_ancestor_Surface.avi

979 Growth of ancestral SBW25 imaged from camera 2.

980

981 Supplementary movie file 2.

982 Name of file: supplementaryMovie2_Wss_Surface.avi

983 Growth of SBW25 Δ*wssA-J* imaged from camera 2.

984

985 Supplementary movie file 3.

986 Name of file: supplementaryMovie3_ancestor_Turbidity.avi

987 Growth of ancestral SBW25 imaged from camera 1.

988

989 Supplementary movie file 4.

990 Name of file: supplementaryMovie4_Wss_Turbidity.avi

991 Growth of Δ*wssA-J* SBW25 imaged from camera 1.

992

993 Supplementary movie file 5.

994 Name of file: supplementaryMovie5_ancestor_ALI.avi

995 Growth of ancestral SBW25 imaged by SLR camera mounted directly above

996 the well.

997

998 Supplementary movie file 6.

999 Name of file: supplementaryMovie6_ancestor_Bioconvection.avi

1000 Replicate of ancestral SBW25 growth imaged by camera 1 with a high
1001 frequency frame rate.
1002
1003 Supplementary movie file 7.
1004 Name of file: supplementaryMovie7_ancestor_Pvd.avi
1005 Growth of ancestral SBW25 imaged from camera 3.
1006
1007 Supplementary movie file 8.
1008 Name of file: supplementaryMovie8_pvd.gif
1009 Simulation of the pyoverdin dynamics.
1010
1011 Supplementary movie file 9.
1012 Name of file: supplementaryMovie9_velocity.gif
1013 Simulation of the velocity dynamics.
1014
1015 Supplementary movie file 10.
1016 Name of file: supplementaryMovie10_biomass.gif
1017 Simulation of the biomass dynamics.
1018
1019
1020 Supplementary movie file 11.
1021 Name of file: supplementaryMovie10_O2.gif
1022 Simulation of the oxygen dynamics.
1023